



Selective reduction of CO₂ by conductive MOF nanosheets as an efficient co-catalyst under visible light illumination

Wei Zhu^{a,b,1}, Chufeng Zhang^{a,b,1}, Qin Li^{a,b}, Likun Xiong^{a,b}, Rongxiang Chen^c, Xiaobing Wan^c, Zhen Wang^d, Wei Chen^e, Zhao Deng^{a,b,*}, Yang Peng^{a,b,*}

^a Soochow Institute for Energy and Materials Innovations, College of Physics, Optoelectronics and Energy & Collaborative Innovation Center of Suzhou Nano Science and Technology, Soochow University, Suzhou 215006, PR China

^b Key Laboratory of Advanced Carbon Materials and Wearable Energy Technologies of Jiangsu Province, Soochow University, Suzhou 215006, PR China

^c College of Chemistry, Chemical Engineering and Materials Science, Soochow University, Suzhou 215123, PR China

^d Thermo Fisher Scientific (China), Guangzhou 510000, PR China

^e Department of Chemistry, National University of Singapore, 117543, Singapore

ARTICLE INFO

Keywords:

CO₂ reduction
Artificial photosynthesis
Nanosheet
2D conductive MOFs
CO₂ fixation

ABSTRACT

Mimicking the natural photosynthesis process, photocatalytic conversion of CO₂ has been an ongoing hotspot of scientific research and technology development. A key aspect is the discovery of high potency catalysts for facilitating the multi-electron participated reactions. Herein we successfully demonstrate exfoliated nanosheets from a conductive 2D-MOF Ni₃(HITP)₂ as an efficient co-catalyst for CO₂ reduction in a hybrid photocatalytic system under visible light illumination. By taking advantage of the high conductivity for charge transportation and highly accessible active sites for redox reactions, an excellent selectivity of 97% for deoxygenative CO₂ reduction and a high CO yield rate of $3.45 \times 10^4 \mu\text{mol} \cdot \text{g}^{-1} \cdot \text{h}^{-1}$ were achieved with superior stability. This work provides essential insights into future design and development of more effective MOFs-based systems for catalytic CO₂ utilization.

1. Introduction

Photocatalytic CO₂ conversion to chemical fuels and feedstock such as CO, methane or other hydrocarbons provides an attractive solution to ease the unsustainable rise of anthropogenic CO₂ emission and energy crisis with two birds killed by one stone [1–5]. Towards this goal, many efforts have been devoted to develop high-efficiency heterogeneous and homogeneous catalysts involving photoactive semiconductors [2,6], metal complexes [7], and carbon nitrides etc [8–12]. However, of the current photocatalytic systems reported for CO₂ reduction, many of them are active only in the ultraviolet region and have shown only limited efficiency and selectivity due to low CO₂ absorption equilibrium, concealed active sites, and competitive hydrogen evolution [3,13–16]. To overcome these limitations, hybrid photocatalytic systems, where the photo-harvesting and electro-catalytic function are undertaken separately by different components, have arisen as an promising approach. Of particular interests, using complexes of Ru-polypyridyl or Ir-phenylpyridine as the photosensitizer, combined with

highly efficient co-catalysts, for CO₂ reduction has been extensively studied [1,17–25]. Significant advances have been made, mainly attributed to a coherent energy transfer from the light absorber all the way to the redox species. Although many catalysts with high turnover frequencies (TOFs) were reported, they still suffer from stability and selectivity issues (Table S1). Therefore, a more efficient exploitation of the photosensitizer by maximizing the potency of the co-catalysts is highly desired due to the noble nature of such photoactive complexes, which in turn requires stronger electron-extracting and catalytic capabilities of the co-catalysts.

Metal-organic frameworks (MOFs), capable of integrating CO₂ capture and its catalytic conversion together, represents a new class of porous materials that can be used in the photocatalytic systems for CO₂ reduction [3,26–29]. Compared to other semiconductors and homogeneous molecular complexes, MOFs catalysts have some intrinsic advantages including high surface area, tunable pore structure, selective gas absorption, and excellent recyclability [26,28–36]. Depending on the photoactive motif, reduction of CO₂ by MOFs can be initiated by

* Corresponding authors at: Soochow Institute for Energy and Materials Innovations, College of Physics, Optoelectronics and Energy & Collaborative Innovation Center of Suzhou Nano Science and Technology, Soochow University, Suzhou 215006, PR China.

E-mail addresses: zdeng@suda.edu.cn (Z. Deng), ypeng@suda.edu.cn (Y. Peng).

¹ These authors contributed equally to this work.

<https://doi.org/10.1016/j.apcatb.2018.07.024>

Received 31 May 2018; Received in revised form 5 July 2018; Accepted 8 July 2018

Available online 10 July 2018

0926-3373/ © 2018 Elsevier B.V. All rights reserved.

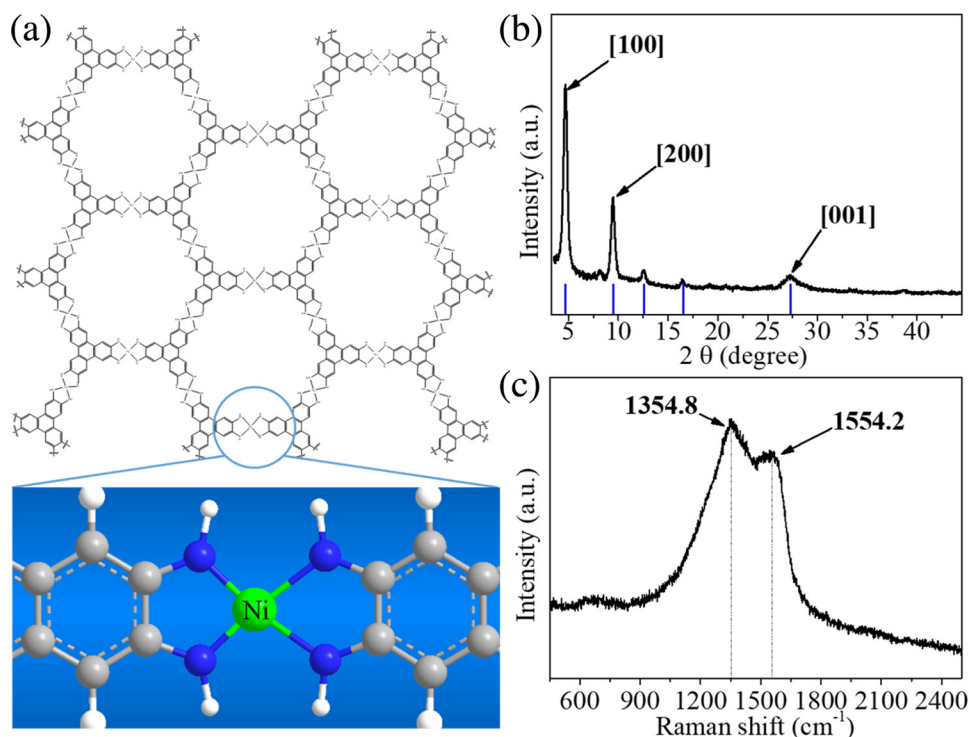


Fig. 1. (a) Coordination structure of $\text{Ni}_3(\text{HITP})_2$; (b) PXRD pattern and (c) Raman spectrum of $\text{Ni}_3(\text{HITP})_2$.

either ligands [37–40] or metal nodes [41–43] or augmented by photo-inactive MOFs as the co-catalyst in the aforementioned hybrid photocatalytic system [44–46]. Tremendous progress have been made in this context, but the lack of structural stability, electric conductivity and electron trap states in conventional MOFs poses a common issue in prohibiting stable and efficient charge transportation and transfer during the photocatalytic cycles.

Particularly, the 2D conductive MOF $\text{Ni}_3(\text{HITP})_2$ (Fig. 1a) with stacked honeycomb lattices has recently drawn great attention by displaying both advantages inherited from the well-defined MOFs structure and the planar Ni-N_4 coordination motif. [47,48] What's more, this class of MOFs is highly conductive, reminiscent of graphene analogue. Measurements on polycrystalline films and pressed pellets recorded a conductivity of greater than 40 S cm^{-1} and 5000 S m^{-1} respectively, [47,49] while the constructed FET read out a hole mobility of $48.6 \text{ cm}^2 \text{ V}^{-1} \text{ s}^{-1}$ [50]. As a result, applications in chemiresistive sensing, super capacitors, and electrochemical oxygen reduction have been successfully demonstrated [48–50]. With the 2D π -conjugated framework and the well-defined Ni-N_4 coordination environment, it is believed even more applications can be realized to take full advantage of the topology, conductivity, and catalytic activity of this class of materials.

With all considerations above, herein we further extend the application of $\text{Ni}_3(\text{HITP})_2$ and explore its potential in photocatalytic reduction of CO_2 in a visible-light photocatalytic system using $[\text{Ru}(\text{bpy})_3]^{2+}$ ($\text{bpy} = 2,2'$ -bipyridine) as the photosensitizer and triethanolamine (TEOA) as the electron donor. By employing the conductive MOF nanosheets as the co-catalyst, this hybrid photocatalytic system demonstrated a high CO yield rate of $3.45 \times 10^4 \mu\text{mol g}^{-1} \text{ h}^{-1}$ with high selectivity of 97% over 3 h. No decay of the MOF catalyst was observed throughout a total of 6 repeated catalytic cycles, displaying excellent stability. The high conductivity, rich Ni-N_4 active sites and 2D nanosheet morphology of the $\text{Ni}_3(\text{HITP})_2$ MOF compose a coherent symphony for realizing its superior catalytic performance.

2. Experimental details

2.1. Materials

Triphenylene was purchased from Accela ChemBio Co., Ltd.. Tris (dibenzylideneacetone) dipalladium ($\text{Pd}_2(\text{dba})_3$) was obtained from BePharm Ltd.. Iron powder (Fe) was purchased from Meryer (Shanghai) Chemical Technology Co., Ltd.. 1, 1'- binaphthyl- 2, 2'- dibenzophenylphosphine (*rac*-BINAP), benzophenone imine ($\text{Ph}_2\text{C} = \text{NH}$), sodium tert-butoxide ($\text{C}_4\text{H}_9\text{ONa}$) and Nickel chloride hexahydrate ($\text{NiCl}_2 \cdot 6\text{H}_2\text{O}$) were purchased from Shanghai Macklin Biochemical Co., Ltd.. Nitrobenzene (PhNO_2), petroleum ether (PE), diethyl ether, ethyl acetate (EA), toluene, liquid bromine (Br_2), acetonitrile (MeCN), ethanol (EtOH), acetone, dichloromethane (CH_2Cl_2), chloroform (CHCl_3), hydrochloric acid (HCl), ammonium hydroxide ($\text{NH}_3 \cdot \text{H}_2\text{O}$) and tetrahydrofuran (THF) were purchased from Sinopharm Chemical Reagent Co., Ltd.. Tris (2, 2'- bipyridyl) dichlororuthenium (II) hexahydrate ($[\text{Ru}(\text{bpy})_3]\text{Cl}_2 \cdot 6\text{H}_2\text{O}$) was purchased from Sigma-Aldrich. All materials were used as received without further purification. The ultrapure water was obtained from the Sartorius, arium mini reinwasser-system. The CO_2 gas (99.995%) was supplied by Suzhou Jinhong Gas Co. Ltd., and the isotopic $^{13}\text{CO}_2$ gas (99.9%) was purchased from Sigma-Aldrich.

2.2. Synthesis

2.2.1. Synthesis of HITP-6HCl

The ligand of 2, 3, 6, 7, 10, 11-hexaaminotriphenylene hexahydrochloride (HITP-6HCl) was prepared according to the previous literature [51,52]. (1) 15 mL of PhNO_2 reaction solution including 4.3 mmol of triphenylene and 1.8 mmol of Fe powder was added into a schlenk tube, and purged with N_2 for 30 min. Then, 2.23 mL of Br_2 was added dropwise into the solution, with the reaction temperature kept at 210°C for 3 h with stirring. After cooling down to room temperature, the solid was filtered and washed with EtOH, acetone and CHCl_3 for several times and the white product 1 was obtained by rotary evaporation. (2) 25 mL of toluene solution containing 0.68 mmol of

$\text{Pd}_2(\text{dba})_3$ and 1.38 mmol of *rac*-BINAP was degassed and purged with N_2 for 15 min, and the solution was kept at 110°C for 30 min with stirring. After cooling down to room temperature, the reactants of 2.85 mmol of the product **1**, 22.7 mmol of $\text{C}_4\text{H}_9\text{ONa}$ and 20.5 mmol of $\text{Ph}_2\text{C}=\text{NH}$ were added gradually, and then the reaction was kept at 110°C for 12 h with stirring. After cooling down to room temperature, the crude products were washed and filtered with CH_2Cl_2 , dried by rotary evaporation. Then the solid was subjected to column chromatography on silica gel with PE:EA (4:1). Finally, the product **2** was collected and evaporated to dryness. (3) 20 mL of THF solution including 0.83 mmol of the product **2** was added into a 2 mL (2.0 M) of aqueous HCl solution dropwise, and the reaction solution was stirred for 30 min at room temperature. The precipitate was isolated by centrifugation and washed with PE for 3 times. After dried in vacuum oven for overnight, the yellow product **3** was obtained, and the yield was about 82%. ^1H NMR ($\text{DMSO}-d_6$): δ (ppm) 7.92 (s, 6H, triphenylene CH).

2.2.2. Synthesis of $\text{Ni}_3(\text{HITP})_2$ nanosheets

The synthesis of bulk $\text{Ni}_3(\text{HITP})_2$ was prepared according to the literature [47]. 0.038 mmol of HITP-HCl was dissolved in 10 mL of ultrapure water to form solution (A), and 0.056 mmol of $\text{NiCl}_2\cdot 6\text{H}_2\text{O}$ was dissolved in another 10 mL of ultrapure water to form solution (B). Then the solution (B) was dropwise added to the solution (A) under stirring. After forming a homogeneous solution, 600 μL of concentrated $\text{NH}_3\cdot\text{H}_2\text{O}$ ($14\text{ mol}\cdot\text{L}^{-1}$) was dropwise added into the above solution, and then the reaction was kept at 65°C with constant stirring under air. After 2 h, black powder, which was produced at the bottom of the beaker, was centrifuged and refluxed in ultrapure water for 24 h (the water was refreshed each 12 h), then the solid was refluxed in acetone for another 3 h. After that, the black powder of bulk $\text{Ni}_3(\text{HITP})_2$ was dried under vacuum at 150°C for 12 h. For exfoliating the bulk $\text{Ni}_3(\text{HITP})_2$ into nanosheets, 30 mg of bulk $\text{Ni}_3(\text{HITP})_2$ was dispersed in 15 mL of acetonitrile, and then sonicated for 24 h.

2.3. Characterization

The crystal structure was characterized by powder X-ray diffraction (XRD, Bruker D8 Advance with $\text{Cu K}\alpha$ radiation ($\lambda = 1.54056\text{ \AA}$)). Fourier transformation infra-red spectrum (FTIR) experiments were carried out on a Nicolet 6700 FT-IR spectrometer. The micro-morphology was observed via a dual-beam electron microscope (SEM, FEI Scios, 20 kV, 0.4 nA) and a field emission transmission electron microscope (TEM, FEI TECNAI G2 F20 200KV). The atomic force microscopy (AFM, Bruker, Dimension Icon) was used to characterize the surface morphology and nanosheet thickness. The chemical states of surface elements was probed by X-ray photoelectron spectroscopy (XPS, Thermo Fisher, Escalab 250Xi), with all binding energy values calibrated by using $\text{C}_{1s} = 284.6\text{ eV}$ as the reference. Ultraviolet photoelectron spectroscopy (UPS) was used to analyze the valence band of the materials, of which the Femi level was calibrated by gold. Raman spectra were obtained on a confocal laser Raman spectrum analysis system (Horiba Jobin Yvon, HR Evolution). Thermal gravimetric analysis (TGA) was performed with EXSTAR 7300 under air atmosphere with a heating ramp of $10^\circ\text{C}/\text{min}$. ^1H nuclear magnetic resonance spectroscopy (^1H NMR) were conducted on a Varian-400 spectrometer. All ^1H NMR spectra were reported as chemical shift δ in units of parts per million (ppm) downfield with reference to deuterated solvent (2.50 ppm for $\text{DMSO}-d_6$). The photoluminescence spectroscopy (PL) was collected on a VARIAN Cary Eclipse spectrometer excited with 370 nm light, and the fluorescence lifetime was collected on a transient spectrofluorometer (Horiba Jobin Yvon) with double exponential fit. The isotope ^{13}C was analyzed by the Mass Spectroscopy (MS, Pfeiffer vacuum Co., OmniStar, GSD 320).

2.4. Photocatalytic activity evaluation

The photocatalytic reduction of CO_2 was carried out in an external irradiation-type reactor (Pyrex glass) with a quartz window on top of the reactor. The reactor was connected to a closed gas-circulation system. The setup of the photocatalytic system is illustrated in Figure S16 in the Supporting Information. Typically, 2 mg of $\text{Ni}_3(\text{HITP})_2$ and 80 mg of photosensitizer $[\text{Ru}(\text{bpy})_3]\text{Cl}_2\cdot 6\text{H}_2\text{O}$ were uniformly dispersed in a solution of TEOA/ H_2O /MeCN (4 mL/2 mL/10 mL) in a petri dish with a diameter of 5 cm by ultrasound, and then the petri dish was placed into the reactor. In order to reduce the evaporation rate of CH_3CN to maintain the solvent volume throughout the photocatalytic process, the reactor was cooled by circulating water to keep the system temperature at 4°C . To ensure the safe operation under a saturating CO_2 environment, after the whole photocatalytic system was completely evacuated for about 10 min to exhaust the air (no O_2 and N_2 is detectable from the gas chromatography), a negative pressure (80 kPa) of pure CO_2 gas was purged into the airtight system, and kept circulating. A 100 W LED light (PLS-LED 100, 420 nm, Beijing Perfectlight science @ technology Co., Ltd.) was used as the light source, and the illumination distance was kept at 7.5 cm from the sample. The gas products (CO , CH_4 , H_2 , O_2 and N_2) were analyzed every 1 h by online gas chromatography (GC 2002, Shanghai Kechuang Chromatograph instruments Co., Ltd.) equipped with a thermal conductivity detector (TCD) and a flame ionization detector (FID), using argon was used as the carrier gas. The quantification of the CO and H_2 was calculated by the calibration curve, with a fitting equation obtained using the external standard method (Figure S17, S18). The solution products in the liquid phase were analyzed by ^1H nuclear magnetic resonance spectroscopy (^1H NMR). To evaluate the cyclability of the catalyst, a partition method was applied to compensate the filtration and transfer loss of the catalyst between each cycles. In details, each cycles we used 2 mg of the MOF catalyst from a total of 20 mg for photocatalysis. After each 2 mg cycle, a parallel experiment was performed for the rest of the catalyst under the same condition. Then all catalysts were mixed together again, and after washing, centrifugation and drying, another 2 mg was taken out for the sequential run until a total of 6 cycles.

2.5. Electrochemical measurements

Electrochemical measurements were performed using a three electrode system connected to an electrochemical workstation (CHI 760E) in an H-cell separated by Nafion 117. The Ag/AgCl electrode serves as reference and the counter electrode is a graphite rod. To prepared the working electrode, 1 mg $\text{Ni}_3(\text{HITP})_2$ was dispersed into 0.25 mL ethanol solution containing 50 μL Nafion solution and 0.5 mg carbon black (Ketjen black). After ultrasound for 60 min, the obtained ink was painted onto the carbon paper (1 cm^2) and then dried in the oven. LSV test was carried out in CO_2 -saturated 0.5 M KHCO_3 solution with a scan rate of $1\text{ mV}/\text{s}$. The gas products were detected by an on-line GC (Agilent 7890B) with a TCD and FID detector, with argon used as the carrier gas.

3. Results and discussion

The structure and purity of the obtained black powder was validated by powder X-ray diffraction (PXRD), X-ray photoelectron spectroscopy (XPS), Raman spectra and Fourier transform infrared spectroscopy (FTIR). The prominent PXRD peaks at $2\theta = 4.7^\circ$, 9.5° , 12.6° , 16.5° and 27.3° match the reported PXRD pattern of $\text{Ni}_3(\text{HITP})_2$ for an eclipsed or slipped-parallel conformation of stacked 2D sheets (Fig. 1b) [47]. Surface atomic chemical states from XPS (Figure S1) reveal C, N, O and split Ni spin-orbit peaks, resulted from the material itself, as well as any adsorbed oxygen species such as H_2O . The binding energies (BE) of Ni (2p) at 855.3 eV and 873.0 eV, and N (1s) at 399.0 eV indicate a single type of Ni and N atoms in the Ni- N_4 four-coordinate structure. No

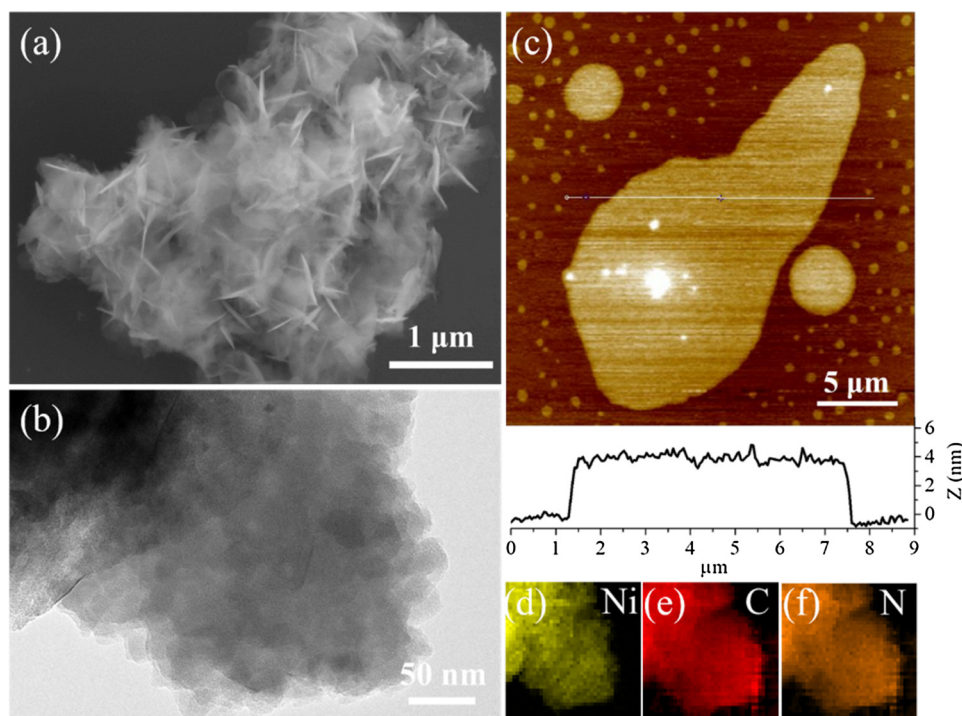


Fig. 2. (a) FESEM and (b) TEM images of $\text{Ni}_3(\text{HITP})_2$; (c) AFM image of $\text{Ni}_3(\text{HITP})_2$ nanosheets; (d–f) Examination of the corresponding EDX mapping reveals the homogeneous distribution of Ni.

impurities of other Ni species such as NiO (853.8 eV), $\text{Ni}(\text{OH})_2$ (855.7 eV) and metallic Ni (852.8 eV) are evident [53–56]. Both of the PXRD and XPS spectra are highly in agreement with those reported by Dincă et al. [47,49,50]. Moreover, additional characterization by Raman (Fig. 1c) revealed two peaks at about 1354.8 and 1554.2 cm^{-1} , reminiscent of the D and G bands of 2D graphitic materials, and FTIR (Figure S2) further confirmed all functional motifs within the MOFs.

The micro-structural and physiochemical properties of the as-synthesized $\text{Ni}_3(\text{HITP})_2$ and exfoliated nanosheets were further examined by FE-SEM, TEM, AFM and TGA. $\text{Ni}_3(\text{HITP})_2$ powders deposited on the silicon wafer clearly show a foliated morphology consisting of two dimensional thin sheets (Fig. 2a), which are further verified by the high-resolution TEM images (Fig. 2b). Elemental mapping indicates the Ni, C and N atoms are homogeneously distributed within the crystalline thin sheets (Fig. 2d–f). Fig. 2c presents an AFM topography image of the exfoliated MOF nanosheets deposited on the silicon substrate. The height profile measures a thickness of 4.2 ± 0.3 nm, indicating the nanosheets are composed of only few layers of the individual 2D MOF plane. With high spatial resolution, these microscopic observations consolidate the previously reported 2D graphene-analogous micro-structure of $\text{Ni}_3(\text{HITP})_2$, in which the HITP ligands are connected to Ni^{2+} centers in a square planar configuration. Thermogravimetric analysis (Figure S3) confirmed our synthesized $\text{Ni}_3(\text{HITP})_2$ is thermally stable up to 330 $^{\circ}\text{C}$, consistent with previous literature report [47], and suitable for most device applications.

The catalytic potency of exfoliated $\text{Ni}_3(\text{HITP})_2$ nanosheets on CO_2 reduction was evaluated in a hybrid photocatalytic system with $[\text{Ru}(\text{bpy})_3]^{2+}$ as the photosensitizer, $\text{Ni}_3(\text{HITP})_2$ as the co-catalyst, TEOA as the electron donor, and a 100 W LED light ($\lambda = 420$ nm) as the light source. Under 80 kPa of CO_2 , 16 mL solutions of $\text{MeCN}/\text{H}_2\text{O}/\text{TEOA}$ (10:2:4 v/v/v) were used as the reaction media, in which various amount of $\text{Ni}_3(\text{HITP})_2$ and $[\text{Ru}(\text{bpy})_3]^{2+}$ were scrutinized for the evolution of both gaseous and liquid reduction products. Under these conditions, CO was detected by gas chromatography (GC) as the major reduction product with a very small amount of H_2 , and no other soluble products such as formate was found by the ^1H nuclear magnetic

resonance spectroscopy (^1H NMR, Figure S4), as formate typically is the most likely reduction product under such conditions [42,57] and its NMR shift should be higher than 10 ppm if detected. The rate of CO evolution is increased with the concentration of the co-catalyst (Figure S5) and the photosensitizer (Figure S6), respectively. Specifically, at a concentration of 2 mg $\text{Ni}_3(\text{HITP})_2$ and 80 mg $[\text{Ru}(\text{bpy})_3]^{2+}$, about 207 μmol CO and only 7.49 μmol H_2 were produced within 3 h, accounting to a yield rate of $3.45 \times 10^4 \mu\text{mol}\cdot\text{g}^{-1}\cdot\text{h}^{-1}$ and selectivity of 97% (Fig. 3a). Such a high yield and selectivity has been rarely seen in literature (Refer to Table S1 for the comparison of Selectivity, TOFs and Quantum efficiencies), and is among the best of reported MOF-based co-catalysts for photocatalytic CO_2 conversion. Under this condition, we conducted all the stability and control studies regarding the hybrid photocatalytic system.

Extending the photoreaction time beyond 4 h (Figure S7), we start to see the rate of CO evolution slows down (a total of 274 μmol was reached after 5 h), possibly due to the deactivation of the photosensitizer. It is well known that in such hybrid photocatalytic systems the deactivation of photo-absorber poses a common issue [45,58], but the deactivation of the co-catalyst also cannot be ruled out. Therefore, in order to investigate whether the slow-down of CO evolution is caused by the deactivation of $\text{Ni}_3(\text{HITP})_2$, we recycled the MOF co-catalyst by filtration (see the photocatalytic test for experimental details) and studied its cycling stability (Fig. 3b). A total of 6 consecutive cycles were carried out using the same catalyst, showing no sign of performance decay. What's more, PXRD and XPS characterizations were performed on the MOFs before and after photocatalysis to verify their structural integrity (Figure S8 and S9). Both of the XRD patterns and XPS spectra reveal no structural change of the $\text{Ni}_3(\text{HITP})_2$ throughout all conducted experimental cycles. Thus, $\text{Ni}_3(\text{HITP})_2$ as a co-catalyst in our hybrid photocatalytic system possesses excellent stability and durability.

Various control experiments were carried out under different conditions to justify the role of $\text{Ni}_3(\text{HITP})_2$ in our photocatalytic system (Figure S10 and S11). First, without using the $\text{Ni}_3(\text{HITP})_2$, there was only 12 μmol CO and 7.46 μmol H_2 produced in 3 h, whereas the

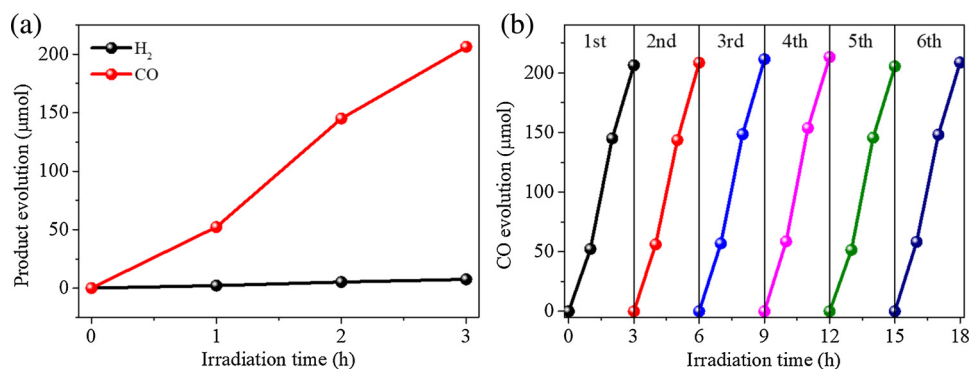


Fig. 3. (a) CO and H₂ evolution vs illumination time of MeCN/H₂O/TEOA solution (16 mL 10:2:4 v/v/v), containing Ru(bpy)₃Cl₂·6H₂O (80 mg) and Ni₃(HITP)₂ (2 mg) under 80 kPa of CO₂ atmosphere at 4 °C; (b) The stability tests of Ni₃(HITP)₂ under the same experimental conditions.

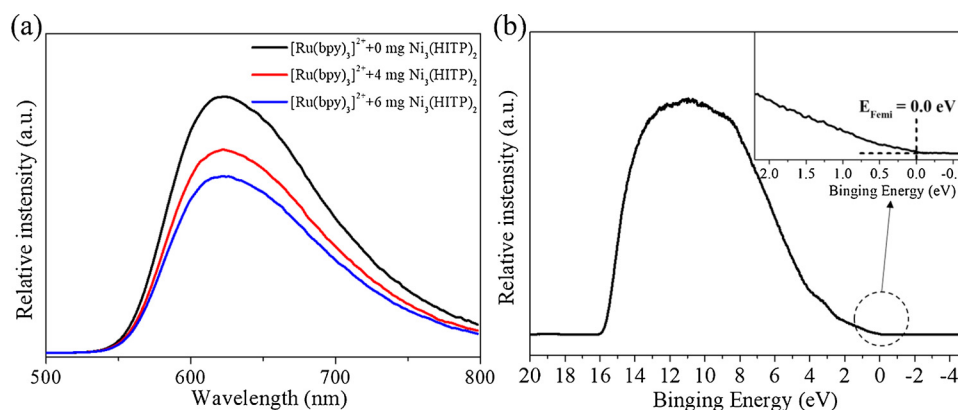
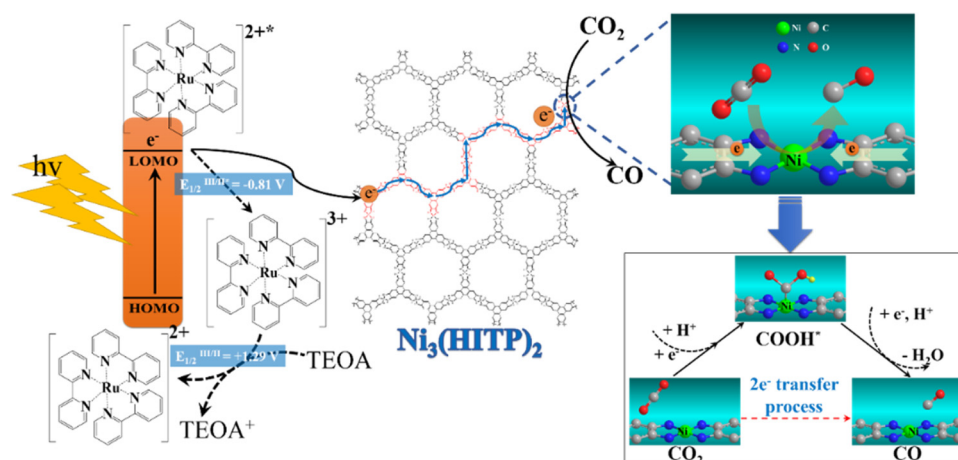


Fig. 4. (a) photoluminescence spectra (PL) of [Ru(bpy)₃]Cl₂·6H₂O with different amount of Ni₃(HITP)₂ powder excited with 370 nm light; (b) Ultraviolet photoelectron spectroscopy (UPS) of the Ni₃(HITP)₂ powder, with the Fermi level calibrated by Au.



Scheme 1. Proposed Mechanism of Photocatalytic CO₂ Reduction to CO with Ni₃(HITP)₂ under Visible-Light Irradiation.

aforementioned complete photocatalytic system containing 2 mg Ni₃(HITP)₂ and 80 mg [Ru(bpy)₃]²⁺ produced 207 μmol CO and only 7.49 μmol H₂. This result indicates that Ni₃(HITP)₂ as the co-catalyst is highly specific for CO₂ reduction, rather than hydrogen evolution. In terms of thermodynamics, upon excited Ru(bpy)₃^{2+*} after accepting one photon, the redox potential $E^{\circ}(\text{Ru(bpy)}_3^{3+}/\text{Ru(bpy)}_3^{2+}) = -0.81 \text{ V vs SCE}$ [1,59] is negative enough to trigger both of the two-electron CO₂ conversion to CO ($\text{CO}_2 + 2\text{H}^+ + 2\text{e}^- \rightarrow \text{CO} + \text{H}_2\text{O}$, $E^{\circ} = -0.36 \text{ V vs SCE}$) and the hydrogen evolution reaction ($E^{\circ} = -0.24 \text{ V vs SCE}$). [15] Thus, the almost exclusive CO₂ activity of the Ni₃(HITP)₂ nanosheets observed in this study must come from the enhanced reaction kinetics, likely due to a higher absorption equilibrium of CO₂ on

the surface of the MOF. To verify this view, first we respectively studied the photocatalytic activities of Ni²⁺ ions and HATP ligands under the same conditions (Figure S10), and observed negligible performance of these two control samples. Second, we investigated the electrocatalytic behavior of the Ni₃(HITP)₂ MOF in a three-electrode electrochemical setup. In the beginning, the same mixed solvent of MeCN/H₂O/TEOA (10:2:4 v/v/v) saturated with CO₂ was used as the electrolyte, but there was barely an exchange current detected due to the insulating nature of such a solvent mixture. We then switched to the CO₂-saturated 0.5 M KHCO₃ solution as the electrolyte, which is typical for electrocatalytic CO₂ reduction. This time a polarization curve was successfully acquired, with a potential onset about -0.3 V vs. RHE and a current

density reaching about 12 mA/cm^2 at -0.8 V (vs RHE). Further GC analysis of the gas product evolution as a function of applied potentials revealed only CO and no H_2 production over the potential range of -0.32 V to -0.72 V (vs RHE) (Figure S12). Although these electrocatalytic experiments were done in a much different condition from that used for photocatalysis, they are able to provide collateral support for the electrocatalytic capability and selectivity of $\text{Ni}_3(\text{HITP})_2$ for CO_2 reduction.

Second, when there was no photosensitizer used in the photocatalytic system, neither CO nor H_2 was detected. This result indicates $\text{Ni}_3(\text{HITP})_2$ alone is not sufficient to trigger the catalytic reaction, suggesting electrons for CO_2 reduction come from photoelectrons generated by the photosensitizer. Third, when the irradiation was cut from the experiments, there was also no detectable CO and H_2 , confirming the reaction is indeed photocatalyzed. Lastly, when there was no supply of CO_2 with all other conditions maintained the same, again no CO was detected except for H_2 ($14 \mu\text{mol}$), indicating that the above produced CO is exclusively from CO_2 . Moreover, isotopic $^{13}\text{CO}_2$ experiments were conducted under identical conditions with reduction products analyzed by GC and mass spectra. A strong peak at $m/z = 29$ (Figure S13), assignable to ^{13}CO , is present in the mass spectra, proofing the carbon source of CO does indeed come from the CO_2 , rather than other organic reagents such as TEOA.

To further interrogate the photocatalytic mechanism, photoluminescence (PL) spectra (Fig. 4a, S14a) and PL decay curves fit to a double exponential model (Figure S14b) were acquired on the photosensitizer $[\text{Ru}(\text{bpy})_3]^{2+}$ together with $\text{Ni}_3(\text{HITP})_2$ in the mixed solvent of MeCN/ H_2O /TEOA. While the characteristic emission peak of the photosensitizer at about 620 nm decreases with increasing $\text{Ni}_3(\text{HITP})_2$, its PL lifetime also decreases with the addition of $\text{Ni}_3(\text{HITP})_2$. These results indicate that the 2D-MOF, owing to its excellent conductivity and ability of electron extraction, enables to quench the irradiated recombination of photogenerated electron-hole pairs on the photosensitizer. Further with ultraviolet photoelectron spectroscopy (UPS), the metallic nature of $\text{Ni}_3(\text{HITP})_2$ was verified (Fig. 4b). The onset of the UPS spectrum (representing the highest occupied state) starts from 0 eV , and is superimposed over the Fermi level of the material calibrated by Au. This dispersive band structure is well agreed with a few previous experimental and theoretical works on the conductivity of $\text{Ni}_3(\text{HITP})_2$, recording a superior conductivity as high as $5000 \text{ S}\cdot\text{m}^{-1}$ [49,60]. As a result, the 2D-MOF serves as an electron reservoir filled by photoelectrons generated by the photosensitizer. In addition, the high surface area of $\text{Ni}_3(\text{HITP})_2$ (up to $630 \text{ m}^2 \text{ g}^{-1}$) [48–50] and its nanosheet morphology provide a large number of exposed catalytic sites easily accessible by solvated CO_2 molecules, and therefore greatly enhance the reaction kinetics. This argument is further supported by a control experiment using the unexfoliated bulk $\text{Ni}_3(\text{HITP})_2$ powder as the co-catalyst, showing a lower catalytic performance ($2.87 \times 10^4 \mu\text{mol}\cdot\text{g}^{-1}\text{h}^{-1}$) than its nanosheet form (Figure S15). What's more, previous studies by density functional theory (DFT) calculations indicate that the isolated Ni-N_4 units throughout the MOF topology are able to provide highly active catalytic sites towards CO_2 reduction by not only facilitating efficient charger transfer, but also lowering the formation energy of intermediates such as COOH^+ [61–63]. This in turn results in higher selectivity for reduction of CO_2 to CO, and inhibits the competitive H_2 evolution simultaneously.

Keeping the above observations and discussions in mind, we propose a reaction scheme as shown in Scheme 1 summarizing the mechanism of photocatalytic cycles in our hybrid CO_2 reduction system. The whole reaction process can be divided into three steps: (1) excitation and electron exchange of the photosensitizer under illumination; (2) the transfer of photogenerated electrons from the photosensitizer to $\text{Ni}_3(\text{HITP})_2$ and their dispersion within the MOF nanosheets; and (3) the catalytic reduction of CO_2 to CO at the Ni-N_4 sites. Specifically, when exposed to light, the sensitizer $[\text{Ru}(\text{bpy})_3]^{2+}$ is excited to $[\text{Ru}(\text{bpy})_3]^{2+*}$, an extremely potent electron donor. At

elevated energy levels, the photoexcited electron of $[\text{Ru}(\text{bpy})_3]^{2+*}$ could be readily delocalized from its π^* orbital and further transferred to the conduction band (CB) of $\text{Ni}_3(\text{HITP})_2$ [59]. Simultaneously, a hole will be left in the HOMO orbital of the sensitizer, accepting an electron from the readily available TEOA with the sensitizer acting as an oxidant [59]. As soon as the photogenerated electron is transferred to $\text{Ni}_3(\text{HITP})_2$, it can be easily dispersed within the conduction band of the MOF nanosheets because of its metallicity [49,60]. Further within the structure of MOF, the electron-rich Ni-N_4 sites promote electrophilic adsorption of CO_2 and H^+ , which adduct to form the COOH^+ as an intermediate by accepting one electron [61–63]. Afterwards, by accepting another electron and H^+ while releasing a H_2O unit, a CO molecule is produced. It is believed that the 2D nanosheet morphology, the high dispersion of electrons enabled by the conductive MOF, plus the localized electron-rich nodes created by the isolated Ni-N_4 units, synergistically promote the above two-electron transfer process.

4. Conclusion

In summary, we have successfully demonstrated the conductive 2D-MOF $\text{Ni}_3(\text{HITP})_2$ in the form of exfoliated nanosheets as an efficient co-catalyst in a hybrid photocatalytic system with $[\text{Ru}(\text{bpy})_3]^{2+}$ as the photosensitizer and TEOA as the electron donor. Under visible light illumination, a high CO yield rate of $3.45 \times 10^4 \mu\text{mol}\cdot\text{g}^{-1}\text{h}^{-1}$ with high selectivity of 97% was achieved for over 3 h. In addition, the cycling experiments with up to 6 repeated cycles, combined with ex-situ PXRD and XPS characterizations, revealed excellent stability and durability of this MOFs-based catalyst. Further through a series of control experiments, together with PL and UPS investigations, a reaction mechanism was proposed with photogenerated electrons from the sensitizer transferred and dispersed into the metallic co-catalyst, and further consumed to reduce CO_2 to CO through a 2-electron transfer process. We believe the excellent catalytic performance of $\text{Ni}_3(\text{HITP})_2$ in the hybrid photocatalytic system studied here is a synergic effect from the high conductivity, the nanosheet morphology and the highly active Ni-N_4 catalytic motif that coexist in this 2D conductive MOF. This work successfully extends the application of 2D conductive MOFs to photocatalytic CO_2 reduction and should shed new light on the design and development of more effective MOFs-based systems for catalytic CO_2 utilization.

Acknowledgments

This work was supported by the 1000 Young Talents Program of China, Natural Science Foundation of China (No. 21701118), Natural Science Foundation of Jiangsu Province (No. K20161209 and No. BK20160323) and the Key Technology Initiative of Suzhou Municipal Science and Technology Bureau (SYG201748). We also extend our sincere appreciation to the support by Suzhou Key Laboratory for Advanced Carbon Materials and Wearable Energy Technologies, Suzhou 215006, China.

Appendix A. Supplementary data

Supplementary material related to this article can be found, in the online version, at doi:<https://doi.org/10.1016/j.apcatb.2018.07.024>.

References

- [1] H. Rao, L.C. Schmidt, J. Bonin, M. Robert, *Nature* 548 (2017) 74–77.
- [2] W. Tu, Y. Zhou, Z. Zou, *Adv. Mater.* 26 (2014) 4607–4626.
- [3] X. Chang, T. Wang, J. Gong, *Energy Environ. Sci.* 9 (2016) 2177–2196.
- [4] S. Xie, Y. Wang, Q. Zhang, W. Deng, Y. Wang, *ACS Catal.* 4 (2014) 3644–3653.
- [5] J.K. Stolarczyk, S. Bhattacharyya, L. Polavarapu, J. Feldmann, *ACS Catal.* (2018) 3602–3635.
- [6] Y. Ma, X. Wang, Y. Jia, X. Chen, H. Han, C. Li, *Chem. Rev.* 114 (2014) 9987–10043.
- [7] A.J. Morris, G.J. Meyer, E. Fujita, *Acc. Chem. Res.* 42 (2009) 1983–1994.

- [8] J. Fu, B. Zhu, C. Jiang, B. Cheng, W. You, J. Yu, *Small* 13 (2017) 1603938–1603947.
- [9] S. Ye, R. Wang, M.-Z. Wu, Y.-P. Yuan, *Appl. Surf. Sci.* 358 (2015) 15–27.
- [10] P. Xia, B. Zhu, J. Yu, S. Cao, M. Jaroniec, *J. Mater. Chem. A* 5 (2016) 3230–3238.
- [11] J. Yu, K. Wang, W. Xiao, B. Cheng, *Phys. Chem. Chem. Phys.* 16 (2014) 11492–11501.
- [12] S. Yin, J. Han, T. Zhou, R. Xu, *Catal. Sci. Technol.* 5 (2015) 5048–5061.
- [13] X. Liu, S. Inagaki, J. Gong, *Angew. Chem. Int. Ed.* 55 (2016) 14924–14950.
- [14] J. Yu, J. Low, W. Xiao, P. Zhou, M. Jaroniec, *J. Am. Chem. Soc.* 136 (2014) 8839–8842.
- [15] S.N. Habisreutinger, L. Schmidt-Mende, J.K. Stolarczyk, *Angew. Chem. Int. Ed.* 52 (2013) 7372–7408.
- [16] H. Chen, C.E. Nanayakkara, V.H. Grassian, *Chem. Rev.* 112 (2012) 5919–5948.
- [17] V.S. Thoi, N. Kornienko, C.G. Margarit, P. Yang, C.J. Chang, *J. Am. Chem. Soc.* 135 (2013) 14413–14424.
- [18] D. Hong, Y. Tsukakoshi, H. Kotani, T. Ishizuka, T. Kojima, *J. Am. Chem. Soc.* 139 (2017) 6538–6541.
- [19] T. Ouyang, H.-H. Huang, J.-W. Wang, D.-C. Zhong, T.-B. Lu, *Angew. Chem. Int. Ed.* 56 (2017) 738–743.
- [20] K. Niu, Y. Xu, H. Wang, R. Ye, H.L. Xin, F. Lin, C. Tian, Y. Lum, K.C. Bustillo, M.M. Doeff, M.T.M. Koper, J. Ager, R. Xu, H. Zheng, *Sci. Adv.* 3 (2017) 1700921–1700930.
- [21] Y. Wang, N.Y. Huang, J.Q. Shen, P.Q. Liao, X.M. Chen, J.P. Zhang, *J. Am. Chem. Soc.* 140 (2018) 38–41.
- [22] T. Ouyang, C. Hou, J.-W. Wang, W.-J. Liu, D.-C. Zhong, Z.-F. Ke, T.-B. Lu, *Inorg. Chem.* 56 (2017) 7307–7311.
- [23] S. Wang, Z. Ding, X. Wang, *Chem. Commun.* 51 (2015) 1517–1519.
- [24] M. Wang, J. Liu, C. Guo, X. Gao, C. Gong, Y. Wang, B. Liu, X. Li, G.G. Gurzadyan, L. Sun, *J. Mater. Chem. A* 6 (2018) 4768–4775.
- [25] S. Wang, B. Guan, X.W.D. Lou, *Energy Environ. Sci.* 11 (2018) 306–310.
- [26] K. Sumida, D.L. Rogow, J.A. Mason, T.M. McDonald, E.D. Bloch, Z.R. Herm, T.-H. Bae, J.R. Long, *Chem. Rev.* 112 (2012) 724–781.
- [27] J.L. White, M.F. Baruch, J.E. Pander III, Y. Hu, I.C. Fortmeyer, J.E. Park, T. Zhang, K. Liao, J. Gu, Y. Yan, T.W. Shaw, E. Abelev, A.B. Bocarsly, *Chem. Rev.* 115 (2015) 12888–12935.
- [28] Y. Chen, D. Wang, X. Deng, Z. Li, *Catal. Sci. Technol.* 7 (2017) 4893–4904.
- [29] M. Wen, K. Mori, Y. Kuwahara, T. An, H. Yamashita, *Appl. Catal. B Environ.* 218 (2017) 555–569.
- [30] D. Wang, R. Huang, W. Liu, D. Sun, Z. Li, *ACS Catal.* 4 (2014) 4254–4260.
- [31] H. He, J.A. Perman, G. Zhu, S. Ma, *Small* 12 (2016) 6309–6324.
- [32] K. Li, B. Peng, T. Peng, *ACS Catal.* 6 (2016) 7485–7527.
- [33] J.-R. Li, J. Sculley, H.-C. Zhou, *Chem. Rev.* 112 (2012) 869–932.
- [34] J.W. Maina, C. Pozo-Gonzalo, L. Kong, J. Schutz, M. Hill, L.F. Dumee, *Mater. Horiz.* 4 (2017) 345–361.
- [35] C.A. Trickett, A. Helal, B.A. Al-Maythaly, Z.H. Yamani, K.E. Cordova, O.M. Yaghi, *Nat. Rev. Mater.* 2 (2017) 17045–17061.
- [36] H. Furukawa, K.E. Cordova, M. O’Keeffe, O.M. Yaghi, *Science* 341 (2013) 1230444–123056.
- [37] C. Wang, Z. Xie, K.E. deKrafft, W. Lin, *J. Am. Chem. Soc.* 133 (2011) 13445–13454.
- [38] K.M. Choi, D. Kim, B. Rungtaweeworant, C.A. Trickett, J.T.D. Barmanbek, A.S. Alshammari, P. Yang, O.M. Yaghi, *J. Am. Chem. Soc.* 139 (2016) 356–362.
- [39] D. Sun, Y. Gao, J. Fu, X. Zeng, Z. Chen, Z. Li, *Chem. Commun.* 51 (2015) 2645–2648.
- [40] M. Wen, K. Mori, Y. Kuwahara, H. Yamashita, *ChemCatChem* 7 (2015) 3519–3525.
- [41] Y. Fu, D. Sun, Y. Chen, R. Huang, Z. Ding, X. Fu, Z. Li, *Angew. Chem. Int. Ed.* 51 (2012) 3364–3367.
- [42] H. Zhang, J. Wei, J. Dong, G. Liu, L. Shi, P. An, G. Zhao, J. Kong, X. Wang, X. Meng, J. Zhang, J. Ye, *Angew. Chem. Int. Ed.* 55 (2016) 14310–14314.
- [43] M.W. Logan, S. Ayad, J.D. Adamson, T. Dilbeck, K. Hanson, F.J. Uribe-Romo, J. Mater. Chem. A 5 (2017) 11854–11863.
- [44] E. Pipelzadeh, V. Rudolph, G. Hanson, C. Noble, L. Wang, *Appl. Catal. B Environ.* 218 (2017) 672–678.
- [45] J. Qin, S. Wang, X. Wang, *Appl. Catal. B Environ.* 209 (2017) 476–482.
- [46] R. Li, J. Hu, M. Deng, H. Wang, X. Wang, Y. Hu, H.L. Jiang, J. Jiang, Q. Zhang, Y. Xie, Y. Xiong, *Adv. Mater.* 26 (2014) 4783–4788.
- [47] D. Sheberla, L. Sun, M.A. Blood-Forsythe, S. Er, C.R. Wade, C.K. Brozek, A. Aspuru-Guzik, M. Dinca, *J. Am. Chem. Soc.* 136 (2014) 8859–8862.
- [48] E.M. Miner, T. Fukushima, D. Sheberla, L. Sun, Y. Surendranath, M. Dincă, *Nat. Commun.* 7 (2016) 10942–10949.
- [49] D. Sheberla, J.C. Bachman, J.S. Elias, C.J. Sun, Y. Shao-Horn, M. Dincă, *Nat. Mater.* 16 (2017) 220–224.
- [50] G. Wu, J. Huang, Y. Zang, J. He, G. Xu, *J. Am. Chem. Soc.* 139 (2017) 1360–1363.
- [51] L. Chen, J. Kim, T. Ishizuka, Y. Honsho, A. Saeki, S. Seki, H. Ihee, D. Jiang, *J. Am. Chem. Soc.* 131 (2009) 7287–7292.
- [52] T. Hirose, Y. Miyazaki, M. Watabe, S. Akimoto, T. Tachikawa, K. Kodama, M. Yasutake, *Tetrahedron* 71 (2015) 4714–4721.
- [53] G.J. Colpas, M.J. Maroney, C. Bagyinka, M. Kumar, W.S. Willis, S.L. Suib, P.K. Mascharak, N. Baidya, *Inorg. Chem.* 30 (1991) 920–928.
- [54] A.N. Mansour, *Surf. Sci. Spectra* 3 (1994) 231–238.
- [55] A.N. Mansour, *Surf. Sci. Spectra* 3 (1994) 211–220.
- [56] A.M. Venezia, R. Bertocello, G. Deganello, *Surf. Interface Anal.* 23 (1995) 239–247.
- [57] S. Wang, W. Yao, J. Lin, Z. Ding, X. Wang, *Angew. Chem. Int. Ed.* 53 (2014) 1034–1038.
- [58] J.-M. Lehn, R. Ziessel, *J. Organomet. Chem.* 382 (1990) 157–173.
- [59] C.K. Prier, D.A. Rankic, D.W.C. MacMillan, *Chem. Rev.* 113 (2013) 5322–5363.
- [60] M.E. Foster, K. Sohlberg, C.D. Spataru, M.D. Allendorf, *J. Phys. Chem. C* 120 (2016) 15001–15008.
- [61] X. Li, W. Bi, M. Chen, Y. Sun, H. Ju, W. Yan, J. Zhu, X. Wu, W. Chu, C. Wu, Y. Xie, *J. Am. Chem. Soc.* 139 (2017) 14889–14892.
- [62] J. Song, E.L. Klein, F. Neese, S. Ye, *Inorg. Chem.* 53 (2014) 7500–7507.
- [63] C. Yan, H. Li, Y. Ye, H. Wu, F. Cai, R. Si, J. Xiao, S. Miao, S. Xie, F. Yang, Y. Li, G. Wang, X. Bao, *Energy Environ. Sci.* 11 (2018) 1204–1210.